

See discussions, stats, and author profiles for this publication at: <https://www.researchgate.net/publication/262772013>

Omnidirectional acoustic absorber with a porous core and a metamaterial matching layer

Article in *Journal of Applied Physics* · May 2014

DOI: 10.1063/1.4876119

CITATIONS

29

READS

498

4 authors, including:



Andrew Stephen Elliott

University of Salford

52 PUBLICATIONS 654 CITATIONS

[SEE PROFILE](#)



Rodolfo Venegas

Universidad Austral de Chile

76 PUBLICATIONS 423 CITATIONS

[SEE PROFILE](#)



O. Umnova

University of Salford

113 PUBLICATIONS 1,290 CITATIONS

[SEE PROFILE](#)

Some of the authors of this publication are also working on these related projects:



EMBED - Embedding measured data with a computational framework for vibroacoustic design [View project](#)



HVAP - Hybrid Virtual Acoustic Prototyping [View project](#)

Omnidirectional acoustic absorber with a porous core and a metamaterial matching layera)

A. S. Elliott, R. Venegas, J. P. Groby, and O. Umnova

Citation: [Journal of Applied Physics](#) **115**, 204902 (2014); doi: 10.1063/1.4876119

View online: <http://dx.doi.org/10.1063/1.4876119>

View Table of Contents: <http://scitation.aip.org/content/aip/journal/jap/115/20?ver=pdfcov>

Published by the [AIP Publishing](#)

Articles you may be interested in

[Analysis of feedback control of piezoelectric transducersa\)](#)

J. Acoust. Soc. Am. **135**, 3425 (2014); 10.1121/1.4875717

[Sound absorption of a finite micro-perforated panel backed by a shunted loudspeakersa\)](#)

J. Acoust. Soc. Am. **135**, 231 (2014); 10.1121/1.4836215

[Thermal boundary layer effects on the acoustical impedance of enclosures and consequences for acoustical sensing devicesa\)](#)

J. Acoust. Soc. Am. **123**, 1364 (2008); 10.1121/1.2832314

[Modal decomposition method for acoustic impedance testing in square ductsa\)](#)

J. Acoust. Soc. Am. **120**, 3750 (2006); 10.1121/1.2360423

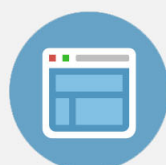
[Near field acoustic holography with particle velocity transducersa\)](#)

J. Acoust. Soc. Am. **118**, 3139 (2005); 10.1121/1.2082687



Re-register for Table of Content Alerts

Create a profile.



Sign up today!



Omnidirectional acoustic absorber with a porous core and a metamaterial matching layer^{a)}

A. S. Elliott,¹ R. Venegas,^{2,1} J. P. Groby,³ and O. Umnova^{1,b)}

¹Acoustics Research Centre, University of Salford, Greater Manchester M5 4WT, United Kingdom

²Carbon Air Ltd., The Innovation Forum, 51 Frederick Road, Greater Manchester M6 6FP, United Kingdom

³LAUM, UMR-6613 CNRS, Université du Maine, Ave. O. Messiaen, 72085 Le Mans, France

(Received 19 February 2014; accepted 30 April 2014; published online 22 May 2014)

An omnidirectional sound absorber based on the acoustic analogy of the electromagnetic metamaterial “black hole” has been developed and tested. The resulting structure is composed of a hollow cylindrical porous absorbing core and a graded index matching layer which employs multiple rods of varying size and spacing to gradually adjust the impedance of the air to that of the porous absorbing core. A semi-analytical model is developed, and the practical challenges and their implications with respect to performance are considered. A full size device is built and tested in an anechoic chamber and the semi-analytical model used in the design process is validated. Finally, the theory is extended to allow for losses in the metamaterial matching layer, and it is shown that improved performance may be achieved with a dual purpose layer which acts as an absorber whilst also providing the required impedance matching condition. © 2014 AIP Publishing LLC. [<http://dx.doi.org/10.1063/1.4876119>]

I. INTRODUCTION

The aim of this work is to design, build and test an omnidirectional sound absorber consisting of a graded-index metamaterial matching layer and a hollow porous core. This structure is the acoustic analogue of the omnidirectional absorber of electromagnetic field (so called “black hole”) described in Ref. 1. It has been shown in this publication that almost complete trapping and further absorption of the incident light can be achieved if the impedance of the surrounding medium is matched to that of the absorbing core by a graded index matching layer with the wave speed linearly decreasing towards the centre of the device.

In graded-index acoustic metamaterials and sonic crystals various sound speed profiles can be achieved by introducing spatial variations of the scattering elements and their arrangement. This property has been utilized in lensing^{2,3} and sound trapping^{4,5} structures.

The ‘black hole’ effect has been already investigated for flexural waves in thin plates for which the required gradual reduction in wave velocity with distance from the edge x can be achieved by changing the plate local thickness as x^m , with $m \geq 2$. This principle has been applied to achieve efficient damping of flexural vibrations in the form of 1D power law wedges with their sharp edges covered by damping materials.⁶ It is shown that ‘black holes’ for flexural waves are capable of efficient absorption of structural vibrations while using only small amounts of attached damping materials which would otherwise have been insignificant.

A number of publications have also appeared since 2011 describing the design of omnidirectional absorbers (OA) of sound. For example, in Ref. 7, a cylindrical device is modeled assuming that the desired sound speed profile in

the matching layer can be achieved by varying the effective bulk modulus while the effective density stays constant (the host medium was assumed to be water in this case). In Ref. 8, a cylindrical OA with an arbitrary contour is proposed with a double negative metamaterial matching layer. In Ref. 9, a small cylindrical device with a matching layer and absorbing core composed of multiple small rods with varying filling fraction was tested. The device was shown to be more effective than the absorbing core alone, absorbing up to 80% of incident energy in the frequency range above 1.2 kHz.

In this work a cylindrical OA is designed for the absorption of low frequency sound, i.e., the range where typical porous sound absorption materials are not effective unless they are very thick. One way to overcome this problem is to use multilayered porous treatments¹⁰ and porous materials with continuous pore stratification¹¹ where a gradual impedance matching with air is achieved.

The idea of combining porous absorbers and metamaterials to improve absorption has become popular in recent years. It has been shown that performance of porous absorbers at low frequencies can be improved by embedding the resonant scatterers.^{12,13} However, the absorption of these structures varies with the angle of incidence.

The design described in this paper is aimed at achieving good absorption at low frequencies irrespective of the angle of incidence. It is based on surrounding the porous absorber by a graded index impedance matching layer, where the impedance matching and the desired wave speed profile are achieved by varying the filling fraction of small scatterers (with radius much smaller than the wavelength of sound); with both their size and the spacing between them being varied. Only a relatively thin layer of common porous absorber (mineral wool) is used for the absorbing core leaving the interior of the structure empty. To validate the model and the design, the full size structure was built and tested in an anechoic chamber.

^{a)}Portions of this paper have been published in Proceedings of Meetings on Acoustics **19**, 065018 (2013).

^{b)}Author to whom the correspondence should be addressed. Electronic mail: o.umnova@salford.ac.uk

The paper is organized as follows. In Sec. II, a semi-analytical model which is used to design the structure is described. In Sec. III, the design of the OA is described. The performance of the optimised structure is compared to that with the approximate matching layer in Sec. IV, where the influence of the porous core thickness and backing conditions on the structure performance are also investigated. In Sec. V, the measurements carried out to validate the model are described. In Sec. VI, the influence of the 3D effects on the data obtained are quantified by comparing it with predictions of 2D and 3D finite element (FE) models of the OA, and the semi-analytical model is validated indirectly by comparing its predictions to those of the 2D FE model. Finally, in Sec. VII, the model is extended to include the viscous and the thermal losses in the matching layer, and the main findings are summarized in Conclusions.

II. THE MODEL

Shown in Figure 1(a) is a cross section of a cylindrical OA, or “black hole,” comprising a metamaterial matching layer (2) and a full porous core (3). In this section of the paper, a 2D semi-analytical model used to design the OA is described.

Consider a cylindrical layer with outer radius R , inner radius R_c , and a radially varying effective density

$$\rho(r) = \rho_0 \alpha(r), \quad (1)$$

and effective bulk modulus

$$K(r) = \rho_0 c^2 \kappa(r). \quad (2)$$

Here, ρ_0 is equilibrium density of air, c is adiabatic speed of sound in air, $\alpha(r)$ and $\kappa(r)$ are normalised effective properties which will be considered in the following. The wavenumber $k(r)$ and the characteristic impedance $Z(r)$ of the layer vary with distance r to the centre as

$$k(r) = k_0 \sqrt{\alpha(r)/\kappa(r)}, \quad Z(r) = Z_0 \sqrt{\alpha(r)\kappa(r)}, \quad (3)$$

where $k_0 = \omega/c$, $Z_0 = \rho_0 c$, and ω is angular frequency of sound. The pressure inside the layer $R_c < r < R$ can be represented as a Fourier series

$$p_L = \sum_{m=-\infty}^{\infty} p_m(r) e^{im(\theta + \frac{\pi}{2})}, \quad (4)$$

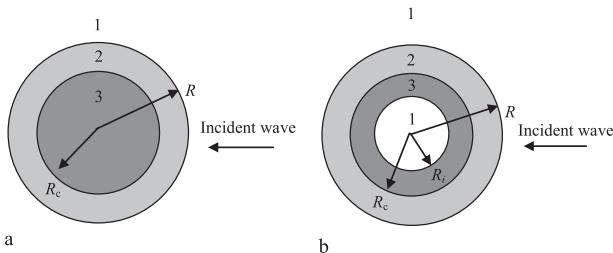


FIG. 1. Cross section of the OA. (a) Full core structure, (b) hollow core structure. 1—air, 2—matching metamaterial layer, 3—porous absorber.

where r and θ are cylindrical coordinates and $p_m(r)$ is the solution of the following equation (derived from equations of momentum conservation $-i\omega\rho(r)\mathbf{v} = -\nabla p$ and mass conservation $-i\omega K(r)p = -\nabla \cdot \mathbf{v}$ written in polar coordinates):

$$\left(r^2 k(r)^2 - m^2\right) p_m + r \left(1 - \frac{r \alpha'(r)}{\alpha(r)}\right) p_m' + r^2 p_m'' = 0. \quad (5)$$

Here, ' stands for differentiation with respect to r and time dependence, in the form $e^{-i\omega t}$, is adopted. When $k(r) = k_0 \sqrt{\alpha(r)}$, i.e., when effective bulk modulus does not vary with radius and $\kappa(r) = 1$, Eq. (5) reduces to that used in the design of the EM black hole for TM polarization.¹ In this case, the simplest capturing profile $k(r) \sim 1/r$ results in $\alpha(r) \sim 1/r^2$, and Eq. (5) can be solved analytically. However, when variations of the effective bulk modulus are not negligible, the analytical solution does not seem possible. In this case, if $k(r) \sim 1/r$, then the dependence $\alpha(r) \sim 1/r^2$ is not achieved as demonstrated below.

Consider a regular array of infinitely long rigid cylinders with radius a and varying filling fraction $F(r)$. For a low frequency wave ($k_0 a \ll 1$) propagating in the plane perpendicular to cylinder axes, this array behaves as a medium with the following effective properties:¹⁴

$$\alpha(r) = \frac{1 + F(r)}{1 - F(r)}, \quad \kappa(r) = \frac{1}{1 - F(r)}. \quad (6)$$

Here, viscous and thermal losses in the array have been neglected, however, their influence will be considered later in Sec. VII. According to Eqs. (6) and (3), the wavenumber and characteristic impedance of the medium vary as

$$k(r) = k_0 \sqrt{1 + F(r)}, \quad Z(r) = Z_0 \frac{\sqrt{1 + F(r)}}{1 - F(r)}, \quad (7)$$

and to achieve $k(r) \sim 1/r$, so that

$$k(r)r = k_0 R, \quad (8)$$

the filling fraction should increase towards the centre of the cylinder as

$$F(r) = \left(\frac{R}{r}\right)^2 - 1, \quad (9)$$

which leads to the following radial dependence of the normalised effective density and bulk modulus

$$\alpha(r) = \frac{\left(\frac{R}{r}\right)^2}{2 - \left(\frac{R}{r}\right)^2}, \quad \kappa(r) = \frac{1}{2 - \left(\frac{R}{r}\right)^2}. \quad (10a)$$

The variations of the characteristic impedance with the radius are described by the following equation:

$$Z(r) = Z_0 \frac{\frac{R}{r}}{2 - \left(\frac{R}{r}\right)^2}. \quad (10b)$$

As $F(r) < F_{cp}$, where F_{cp} is close packing filling fraction, the inner radius of the matching layer has a lower bound: $R_c > \frac{R}{\sqrt{1+F_{cp}}}$.

Substituting (8) and (10a) in (5), the following equation for functions p_m in series (4) is derived:

$$(R^2 k_0^2 - m^2)p_m + r \frac{6r^2 - R^2}{2r^2 - R^2} p'_m + r^2 p''_m = 0, \quad (11)$$

Pressure variations inside the full porous absorbing core (Figure 1(a)), $r < R_c$, and outside the device, $r > R$ are described as

$$p_p^{full} = \sum_{m=-\infty}^{\infty} A_m J_m(k_p r) e^{im(\theta + \frac{\pi}{2})}, \quad (12a)$$

$$p_{out} = \sum_{m=-\infty}^{\infty} (J_m(k_0 r) + B_m H_m(k_0 r)) e^{im(\theta + \frac{\pi}{2})}, \quad (12b)$$

where k_p is wavenumber of the porous material and J_m is Bessel function of the first kind of order m . An incident plane wave with a unit amplitude is assumed.

The scattering coefficients A_m and B_m are defined from matching the pressure and radial particle velocity component on the absorber/matching layer interface R_c and the structure outer radius

$$A_m J_m(k_i R_c) = p_m(R_c), \quad (13a)$$

$$\frac{A_m}{\alpha_p} J'_m(k_i R_c) = \frac{1}{\alpha(R_c)} p'_m(R_c), \quad (13b)$$

$$J_m(k_0 R) + B_m H_m(k_0 R) = p_m(R), \quad (13c)$$

$$J'_m(k_0 R) + B_m H'_m(k_0 R) = p'_m(R), \quad (13d)$$

where α_p is normalised effective density of a porous absorbing material. It is then convenient to introduce the function $q_m(r) = p'_m(r)/p_m(r)$, so it is then followed from Eqs. (13c) and (13d) that

$$B_m = \frac{q_m(R) J_m(k_0 R) - J'_m(k_0 R)}{H'_m(k_0 R) - q_m(R) H_m(k_0 R)}, \quad (14)$$

where $q_m(R)$ is calculated from the following equation (obtained from (11)):

$$q'_m + q_m^2 + \frac{6r^2 - R^2}{(2r^2 - R^2)r} q_m + \frac{(k_0 R)^2 - m^2}{r^2} = 0, \quad (15)$$

with a boundary condition which follows from (13a) and (13b)

$$q_m(R_c) = \psi_m = \frac{\alpha(R_c) J'_m(k_p R_c)}{\alpha_p J_m(k_p R_c)}. \quad (16)$$

Equation (15) is solved numerically using explicit finite difference scheme.

If the absorbing core is hollow (as shown in Figure 1(b)), so the porous absorber has thickness l ; inside the porous layer, $R_i \leq r \leq R_c$, where ($R_i = R_c - l$) the pressure is given by

$$p_p^{hollow} = \sum_{m=-\infty}^{\infty} (C_m J_m(k_p r) + D_m H_m(k_p r)) e^{im(\theta + \frac{\pi}{2})}, \quad (17)$$

and in the inner part of the structure, $r \leq R_i$, the pressure is

$$p_{in} = \sum_{m=-\infty}^{\infty} E_m J_m(k_0 r) e^{im(\theta + \frac{\pi}{2})}. \quad (18)$$

A porous layer could have no backing or perhaps be rigidly backed depending on the application. Thus, in the first case, boundary conditions of pressure and radial velocity continuity at $r = R_c$ and $r = R_i$ would be applied to calculate the scattering coefficients B_m , and, in the second case, a zero radial velocity condition is applied at $r = R_i$. As a result, the scattering coefficients are calculated using the existing Eqs. (14) and (15), however the boundary condition (16) should be replaced by the following one:

$$q_m(R_c) = \psi_m \frac{J_m(k_p R_c)}{J'_m(k_p R_c)} \cdot \frac{J'_m(k_p R_c) + d_m H'_m(k_p R_c)}{J_m(k_p R_c) + d_m H_m(k_p R_c)}, \quad (19)$$

where, for an open layer,

$$d_m = - \frac{J_m(k_p R_i) J'_m(k_0 R_i) - \alpha_p J_m(k_0 R_i) J'_m(k_p R_i)}{H_m(k_p R_i) J'_m(k_0 R_i) - \alpha_p J_m(k_0 R_i) H'_m(k_p R_i)}, \quad (20)$$

and, for a rigidly backed layer,

$$d_m = - \frac{J'_m(k_p R_i)}{H'_m(k_p R_i)}. \quad (21)$$

The porous absorber outer radius R_c should be defined from impedance matching condition between the matching layer and the porous absorber. Using Eq. (10b), the following expression is derived:

$$R_c = \frac{R}{\sqrt{2}} \frac{\sqrt{8|z_p|^2}}{\sqrt{1 + 8|z_p|^2} - 1}, \quad (22)$$

where z_p is the normalised characteristic impedance of the porous absorber. It was chosen here to match the absolute value of the porous material impedance. Matching its real part would lead to a slightly different value of R_c and to slight variations in the matching layer filling fraction profile.

III. DESIGN CONSIDERATIONS

A. Structure size and working frequency range

According to Ref. 1, an OA for electromagnetic waves is efficient when its size exceeds the wavelength of the radiation. However, if low frequency sound is to be absorbed, this

would result in an impractically large structure. In this work, a limit on the external radius of the structure was chosen to be $R = 75$ cm for practical reasons. The radius R was, therefore, roughly equal to the wavelength of sound with frequency 460 Hz. The upper boundary of the working frequency range is defined by the size of the rods used in the matching layer, so that they remain small compared to wavelength, i.e., $k_0 a \ll 1$. The largest size rods used in the experiment have radius $a = 0.635$ cm, so, for the matching layer to act as an effective medium, frequency should be much lower than 8597 Hz. This condition is satisfied in the experiments where the highest frequency is 1000 Hz.

B. Porous absorber properties

The characteristic impedance and wavenumber of mineral wool were measured in the impedance tube using a standard method¹⁵ and the equivalent fluid model^{16,17} for rigid porous material was used to calculate the normalised effective density $\alpha_p(\omega)$ and bulk modulus $\kappa_p(\omega)$ of the porous layer according to

$$\alpha_p(\omega) = \rho_0 \frac{\alpha_\infty}{\phi} \left(1 + \frac{\sigma \phi}{-i\omega \rho_0 \alpha_\infty} \sqrt{1 - i\omega \frac{4\rho_0 \eta \alpha_\infty^2}{\sigma^2 \phi^2 \Lambda^2}} \right), \quad (23a)$$

$$\kappa_p(\omega) = \frac{1}{\phi} \left(\gamma - \frac{\gamma - 1}{1 + \frac{\eta \phi}{-i\omega N_{pr} \rho_0 \kappa_0'} \sqrt{1 - i\omega \frac{4N_{pr} \rho_0 \kappa_0'^2}{\eta \phi^2 \Lambda'^2}}} \right)^{-1}, \quad (23b)$$

where η is the coefficient of dynamic viscosity of air, γ is the adiabatic constant, $N_{pr} = \eta c_p / \kappa$ is the Prandtl number (approximately equal to 0.71 in air at normal conditions), c_p is the heat capacity of air at constant pressure, and κ is the coefficient of thermal conductivity. The six material parameters required by the model are: α_∞ the tortuosity, ϕ material porosity, σ the flow resistivity, κ_0' the thermal permeability, and Λ and Λ' the characteristic viscous and thermal lengths. Viscous losses in porous material are accounted for in expression (23a), while those due to heat transfer between

the air and the solid are taken into account in the expression for the normalised bulk modulus (23b).

The porosity value ($\phi = 0.96$) was deduced from density measurements assuming that the solid frame density is equal to that of quartz. The flow resistivity $\sigma = 33\,726$ Pa s/m² was measured in the standard test. Other parameters required the model adjusted to fit the impedance and wavenumber data (Figures 2(a) and 2(b)) in the frequency range of 400 Hz–1100 Hz. This resulted in the following values: $\alpha_\infty = 1.04$, $\kappa_0' = 10^{-9}$ m², $\Lambda = 24 \times 10^{-6}$ m, $\Lambda' = 47 \times 10^{-6}$ m. The calculations of the absorbing core radius R_c were performed using Eq. (22) and assuming characteristic impedance matching at 1000 Hz which gives $R_c = 62.5$ cm. The filling fraction of rods in the matching layer at this location is equal to 0.44. The choice of the matching frequency was somewhat arbitrary, however, as any frequency in the chosen working frequency range could have been selected. The sensitivity of the device's performance in this respect shall be discussed in Sec. IV.

C. Approximation of the matching layer

The filling fraction profile in the matching layer defined by Eq. (9) was approximated using 6 rows of small cylinders. This provides a staircase approximation of a continuous profile as shown in Figure 3(a). The cylinders were distributed equally over the circumference of each layer. Each layer is characterised by its lattice constant and the number of cylinders in it. These two parameters were chosen so that the desired filling fraction of cylinders in each layer was achieved. The diameter of the rods was between 0.8 cm and 1.3 cm. For the outer layer, 4 mm radius rods at 2.3 cm centre-to-centre distance were used, and for the sixth layer, 0.64 cm rods at 1.7 cm centre-to-centre distance. The lowest filling fraction, in the outer layer, was 0.09, and the outer radius of this layer was approximately 74 cm (see Table I). A cross section of the structure is shown in Figure 3(b).

IV. PERFORMANCE CHARACTERIZATION

In this section, the implications of the design considerations outlined in Sec. III are summarized, and the procedure for evaluating performance of the OA is outlined. In

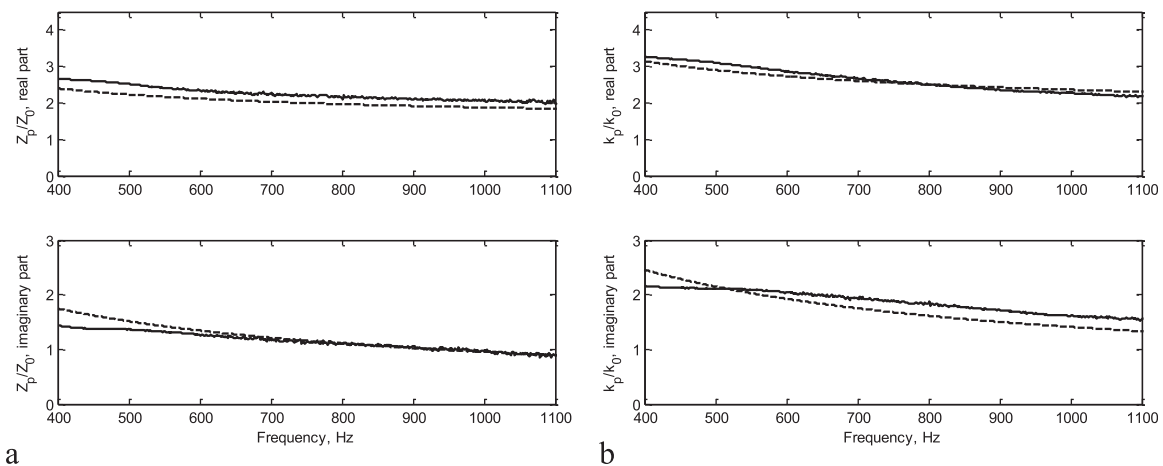


FIG. 2. Characteristic impedance (a) and wavenumber (b) of the mineral wool. Solid line: data, dashed line: equivalent fluid model.

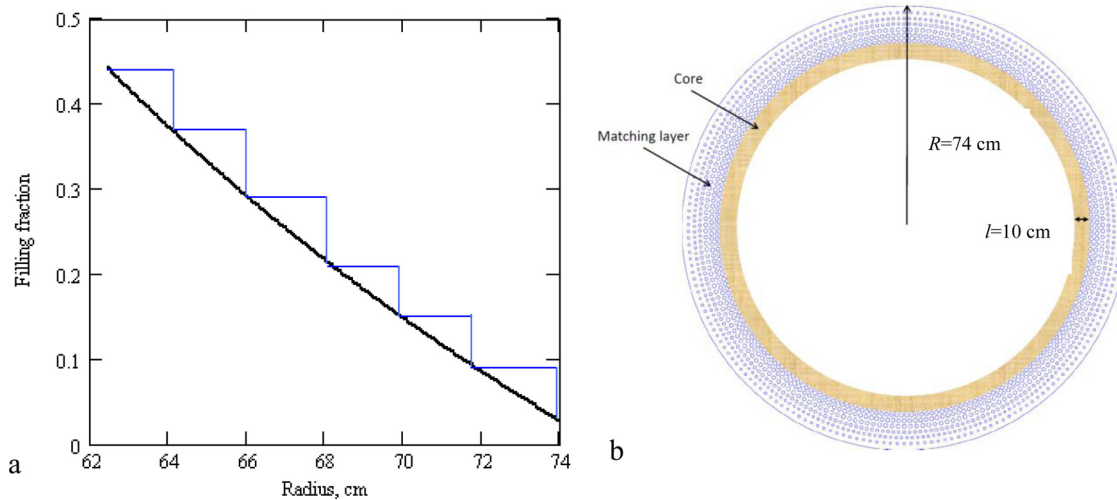


FIG. 3. (a) Continuous profile of the filling fraction in the matching layer (Eq. (9)) and its approximation. Parameters of 6 rows of small cylinders are given in Table I. (b) Cross section of OA: 6 rod layers and 10 cm mineral wool absorbing layer.

particular, the effect on performance due to approximations to the matching layer and the thickness of the absorbing core layer are discussed.

A. Performance descriptors

Several properties can be used to describe the performance of a finite size absorber, assuming that its main function is to minimise front reflections while keeping low pressure levels behind (shadow zone). Here, four performance descriptors are used: Angle averaged energy reflection coefficient of the frontal zone, angle averaged insertion loss (IL) of the shadow zone, angular distribution of the normalised pressure amplitude on the absorber surface, and the absorption cross section per unit length of the cylinder.

The angle averaged energy reflection coefficient,

$$|R|^2 = \frac{1}{\pi} \int_{-\pi/2}^{\pi/2} \left| \frac{p_t - p_i}{p_i} \right|^2 d\theta, \quad (24)$$

where $p_{i,t}$ are pressures on the absorber surface in free field and with the absorber installed, characterizes the reduction of reflections at the front surface of the absorber.

In the shadow zone, the angle averaged insertion loss (IL),

$$IL = \frac{-20}{\pi} \int_{\pi/2}^{3\pi/2} \log_{10} \left(\left| \frac{p_t}{p_i} \right| \right) d\theta, \quad (25)$$

TABLE I. Parameters of 6 rows of cylinders used to approximate the matching layer.

Layer number	Inner radius (cm)	Filling fraction	Effective layer thickness (cm)	Rod radius (cm)	Number of rods
1	62.43	0.44	1.69	0.635	235
2	64.12	0.37	1.86	0.635	220
3	65.98	0.29	2.08	0.635	202
4	68.06	0.21	1.82	0.476	238
5	69.88	0.15	1.82	0.4	245
6	71.70	0.09	2.31	0.4	199

is used to provide information about the quality of the geometrical shadow of the structure. The IL is calculated as the difference between the sound pressure level with and without the structure present. Obviously, a low pressure level at a specific distance from the absorber does not necessarily mean that it is low everywhere else behind it. To overcome this, 2D maps of pressure distributions will also be plotted.

The angular distribution of pressure amplitude on the absorber surface gives a visual representation of its quality. If the pressure amplitude, normalised to that of the incident wave, is close to unity everywhere in the front zone, this means that reflections are successfully eliminated. Behind a good absorber, this quantity should be as close to zero as possible.

Finally, according to Eq. (21) from Ref. 18, the absorption cross section per unit length of a cylinder can be defined as the absorbed power, divided by the intensity of the incident plane wave and is calculated as

$$Q = \frac{-4 \sum_{m=-\infty}^{\infty} (|B_m|^2 + \text{Re}(B_m))}{k_0}. \quad (26)$$

This quantity has been used to characterize the performance of electromagnetic OA in Ref. 19. In acoustics, it has been used to describe the absorption by, for instance, porous cylinders.¹⁸ However, this descriptor should be used with caution as the predicted and measured absorption cross section per unit length can exceed the actual cylinder diameter, due to the so called “edge effect.”²⁰ This happens predominantly around resonant frequencies of the structure, however, “edge effects” are noticeable at other frequencies too. Consequently, absorption cross section does not always represent a physically meaningful quantity when applied to the structures comparable in size to the wavelength of the incident sound. For this reason, it is used here only to compare the efficiency of the device with that of the porous core alone.

B. Influence of the matching layer approximation—full porous core

To emphasize the effect of the matching layer, the performance of the OA must be compared with that of the porous cylinder made of the same mineral wool as the absorbing core and of the same size as the OA itself. This is to provide a point of reference against which the performance of the OA is evaluated.

However, as described in Secs. III B and III C, in real device, the matching can be achieved at just one frequency in the working range. Due to frequency dependence of the porous absorber's impedance and wavenumber, satisfying the matching condition (22) would require different matching layer profiles and porous core radii for different frequencies which is impossible to achieve in practice. For this reason, in this Section, the performance characteristics of the structure with “approximate” matching (i.e., matching achieved at 1000 Hz as explained in Sec. III B) will also be compared to that of the “optimised” device, in which the matching layer profile and core radius have been calculated to achieve impedance matching at the frequency of the incident wave (i.e., tuned to the frequency of the incident wave). This is done in order to estimate the deterioration in performance due to approximate matching.

The calculations for the structure with “approximate” matching have been performed assuming multilayered cylinder with 6 outer layers and a full mineral wool absorbing core. It was assumed that each layer is characterised by its effective wavenumber and characteristic impedance defined by Eq. (7). Thicknesses of the layers and filling fractions of rods in each of them are given in Table I. Note, that the “approximate” structure radius (74 cm) is less than that of the “optimised” device as the minimum filling fraction in the outer layer was nonzero.

The angular distribution of *rms* pressure on the surfaces of three structures (i.e., “approximate” device, “optimised” device and porous cylinder) normalised to that in the free field is shown in Figures 4(a)–4(c) for frequencies 300 Hz, 500 Hz, and 1000 Hz. A plane wave incident from the right is assumed. An “optimised” device providing impedance matching at these frequencies would have absorbing core radii R_c of 59 cm, 60 cm, and 62.5 cm with maximum filling

fractions in the matching layer of 0.62, 0.54, and 0.44, respectively. Absorbing core radii, R_c , have been calculated using Eq. (22) with mineral wool impedance values corresponding to 300 Hz, 500 Hz, and 1000 Hz. Equation (9) with $r = R_c$ has been used to calculate the maximum filling fractions in the matching layer.

At frequencies 300 Hz and 500 Hz, the differences in the performance of the “approximate” and “optimised” devices are due to two factors. The first factor is the impedance mismatch between the core and the matamaterial layer at $r = R_c$, while the second one is the staircase approximation of the matching layer profile. At 1000 Hz, the differences are due solely to the staircase approximation of the matching layer profile. The pressure on the front surface of the structures with “optimised” and “approximate” matching profiles is close to one, which indicates reduced reflections, while considerable frontal reflections are observed from the porous cylinder without the matching layer. Behind the structure, pressure becomes lower as frequency increases and the wavelength become shorter.

The energy reflection coefficient averaged over the front zone defined by Eq. (24) is shown for frequencies in the range of 300 Hz–1200 Hz in Figure 5(a), and the IL averaged over the shadow zone behind the cylinder defined by Eq. (25) is shown in Figure 5(b). For both “optimised” and “approximate” structures, the front zone reflection coefficient is lower than that of the porous cylinder alone.

The “optimised” structure provides less backscattering (higher IL) than the “approximate” one. However, below 700 Hz, the front reflections are significantly reduced, while the sound level reduction in the shadow zone of the “approximate” structure is higher than that of the porous absorber alone.

C. Influence of the porous core thickness

In this section, the performance of the structure with a hollow porous core is compared to that with a full core. The calculations are performed for the structure with an “approximate” matching layer profile. To emphasize the effect of the matching layer, comparisons are also performed with a hollow porous cylinder made of the same mineral wool as the absorbing core and equal in size to OA.

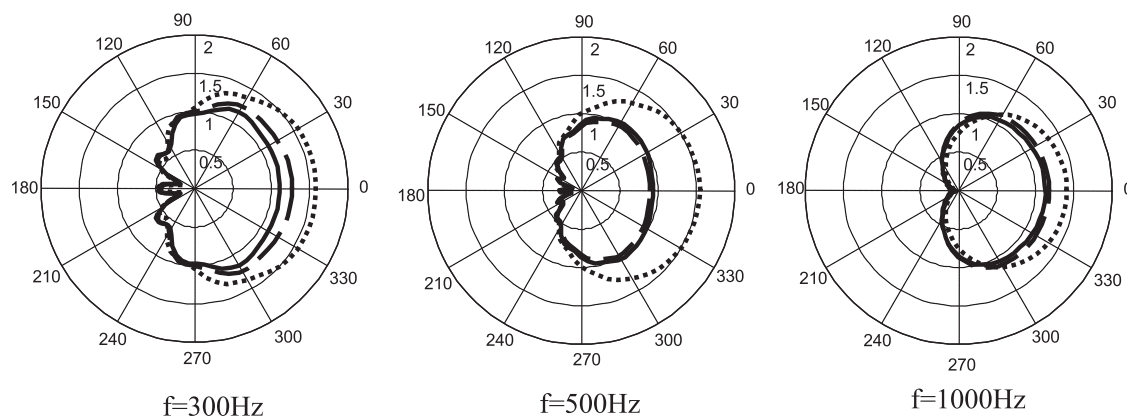


FIG. 4. Angular distribution of normalised *rms* pressure on the surface. Solid line: “optimised” OA with full core, $R = 75$ cm, dashed line: OA absorber with “approximate” matching layer profile (Table I) and full core, dotted line: porous cylinder, $R = 75$ cm.

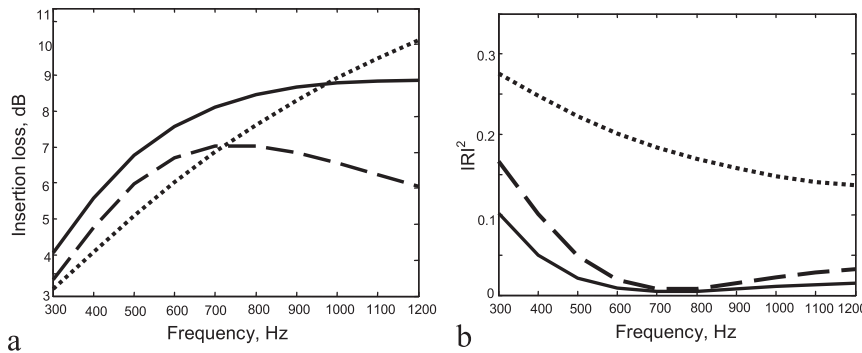


FIG. 5. Angle averaged insertion loss behind the absorber (a), angle averaged energy reflection coefficient of the front absorber surface (b). Legend as in Figure 4.

In Figure 6(a), the radial pressure distribution on the surface of the structure is shown for two different thicknesses of porous absorbing core at 500 Hz. The pressure on the surface of the hollow porous cylinder is shown for comparison. In Figure 6(b), the distributions are shown for a structure with hard backed porous absorbing core and a hard-backed hollow porous absorber.

It is clear that the OA is efficient only when the absorbing core is not too thin because for a 3 cm thick core the structure reflects a significant proportion of the incident radiation. However, it is still more efficient than the hollow porous cylinder. For a thickness of 10 cm, however, the pressure distribution on the surface of the device with the hard-backed core is very close to that with an open core, making its efficiency independent on the boundary condition at the inner porous core surface. In the following, the performance of the device with 10 cm open porous core will be investigated.

In Figures 7(a) and 7(b), the angle averaged energy reflection coefficient of the front surface (24) and the angle averaged IL (25) behind the structures with hollow porous core of thickness 10 cm are compared with those for the structure with the full porous core and for the hollow porous cylinder with 10 cm thickness in the frequency range of 300 Hz–1200 Hz. It can be seen that the IL behind the structure decreases at low frequencies if a hollow core is used, while its values at higher frequencies are not that strongly affected by the absorber thickness. Compared to a hollow porous cylinder, the frequency (300 Hz–1200 Hz) averaged value of reflection coefficient $|R|^2$ is reduced by 78% for OA with 10 cm hollow porous core. As to the IL, its frequency averaged value is 12% lower for the OA with 10 cm porous

core compared to that of the hollow porous cylinder alone. Improvements in the IL values are achieved below 730 Hz.

It can be concluded that the efficiency of the OA with 10 cm porous core is close to that with the full core and that decreasing the absorber thickness to 3 cm leads to strong deterioration in performance.

The absorption cross section per unit length of the structure with 10 cm porous core, calculated using Eq. (26), is 150 cm at 300 Hz, 161 cm at 500 Hz, 158 cm at 700 Hz, and 145 cm at 1000 Hz. These values are between 97% and 107% of the structure diameter (150 cm) and between 116% and 129% of the absorbing core diameter (125 cm). This confirms that in this frequency range, the structure absorbs nearly all sound incident on its surface despite the fact that no absorption is happening in the matching layer.

V. MEASUREMENTS

In order to test the performance of the OA described in Secs. II–IV, a physical prototype was constructed and installed in the anechoic chamber of the University of Salford, UK. This particular chamber provided a near reflection free environment above 100 Hz and a low background noise level for the tests. The completed OA was 125 cm in height and 148 cm in diameter as shown in Figures 8(b) and 3(b), respectively. An omnidirectional sound source (dodecahedron), visible in Figure 8(a), was positioned at a distance 187 cm from the device surface. The plan view of the experimental set up is shown in Figure 8(c). 40 microphones were equally distributed around the surface of the tested structure.

In addition to the tests on the omnidirectional absorber, two additional experiments were also carried out. The first of

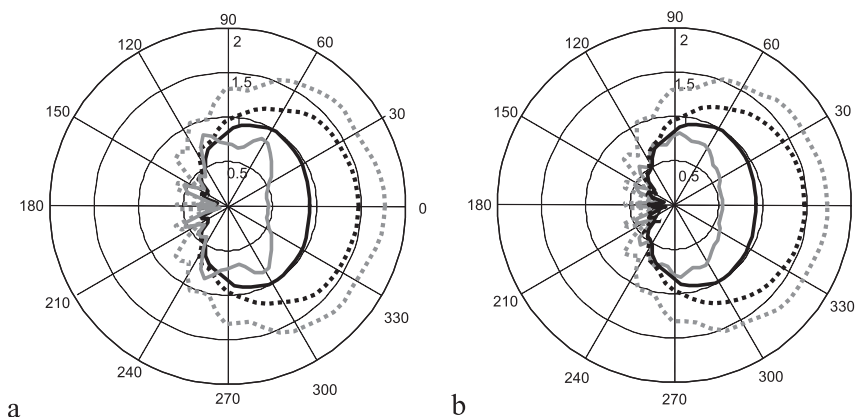


FIG. 6. Angular distribution of normalised *rms* pressure on the surface of the OA with hollow open (a) and hard-backed (b) porous core, frequency 500 Hz. Solid line: OA with hollow core, dotted line: hollow porous cylinder with radius 75 cm. Dimensions of the matching layer as in Table I, plane wave incident from the right. Porous absorber thickness: black lines: 10 cm, grey lines: 3 cm.

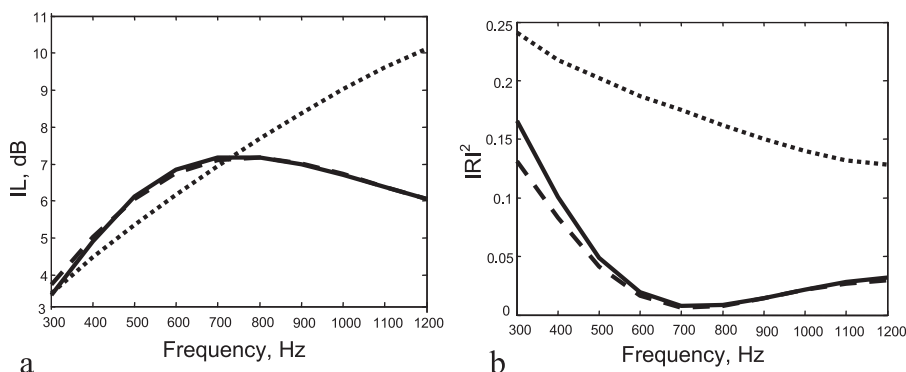


FIG. 7. Angle averaged insertion loss behind the absorber (a), angle averaged energy reflection coefficient of the front absorber surface (b) Solid line: structure with full porous core, dashed line: structure with hollow open porous core, thickness 10 cm, dotted line: hollow porous absorber cylinder without matching layer.

these tests was performed on the framework of the OA so that any influence could be understood and if necessary accounted for. This is important because of the finite height of the device; the semi-analytical model used in the design process assumed infinite height, and, as a result, there may be a discrepancy between measurement and model prediction. The second additional test was performed using this same framework but lined with a 10 cm layer of mineral wool as shown in Figure 3(a). This structure was tested to provide a point of reference against which the performance of the OA can be compared. Since the same porous absorber was used for the mineral wool cylinder and for the OA core, the difference between these measurements can be attributed to the use of the matching layer. The outer dimensions of the OA and the mineral wool cylinder were the same, so the amount of absorber material was slightly less for the OA because of the matching layer, see Figures 3 and 8.

From these three test setups, three independent data sets were obtained:

1. 40 sound pressure readings p_f measured on the surface of the frame structure,
2. 40 sound pressure readings p_m measured on the surface of the mineral wool cylinder,
3. 40 sound pressure readings p_b measured on the surface of the OA.

The acoustic excitation, pink noise from the omnidirectional sound source, was the same in each instance, and the 40 microphone positions were constant for each structure tested in so far as that was possible.

VI. MODEL VALIDATION

In order to comprehensively validate the 2D semi-analytical model based on a 3D experiment, an intermediate step was taken. This step required the development of two FE models (3D and 2D) of the device. The 3D model was designed to mimic as closely as possible the experimental setup, i.e., the physical positioning of the source and supporting plates were replicated.

In the 3D model, the supporting plates were modeled as perfectly reflecting surfaces virtually placed in a spherical fluid domain, and an outer spherical shell was used to simulate the anechoic condition found in the chamber. The sound source was modeled as a point source. The 2D model can be considered as a free field condition since the supporting plates are not included in the model. Thus, the 2D geometry consisted of two concentric circles with the outer one being set as perfectly-matched layer.

In both cases, 3D and 2D, normal temperature and atmospheric condition were considered, and the wave equation was solved using the finite element solver Comsol

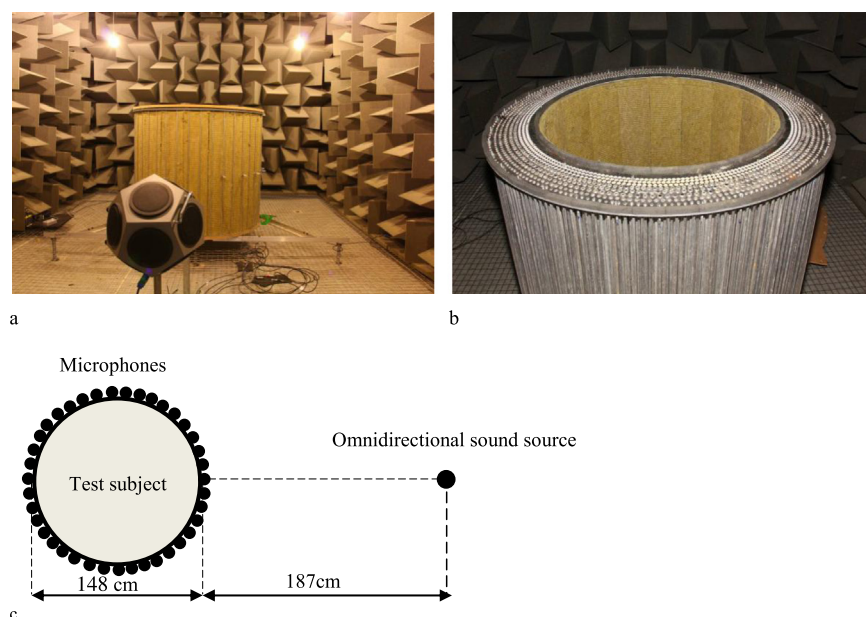


FIG. 8. Mineral wool hollow cylinder installed in the anechoic chamber (a). In the foreground of the image is the omni-directional sound source (dodecahedron) used for the acoustic excitation. The aluminium rods forming the frame were used as the microphone attachment points. The interior of the OA showing matching layer (rods) and hollow absorbing core (mineral wool) (b). Plan view of the experimental set up (c). 40 microphones were equally distributed around the surface of the test subject.

Multiphysics. Before plotting, the data were normalised to the absolute pressure measured (physically and virtually) at the front microphone. As shown in Figure 9(a), the free field data at 300 Hz, 500 Hz, 800 Hz are close to the predictions of the 3D FE model (including supporting plates) and deviate strongly from those of 2D due to the presence of the boards.

Pressure distributions p_m measured on the surface of the hollow absorbing cylinder and p_b measured on the surface of the OA are not significantly affected by the supporting plates. This is demonstrated in Figure 9(b), where the *rms* pressure for the OA normalised to the front microphone reading is shown.

As before, the 3D model mimics the experimental setup, and the core material has been modeled as an equivalent fluid using Eq. (23) of Johnson–Allard model.^{16,17} The layers composing the matching layer were modeled as an equivalent fluid with effective density and bulk modulus calculated using Eq. (23). The parameters for each layer were calculated as functions of the filling fraction F and cylinder radius a using the values shown in Table I. In the medium composed of identical circular cylinders arranged perpendicular to sound propagation direction, parameters in Eq. (23) can be approximated from the knowledge of the cylinder radius a and porosity $\phi = 1 - F$ using Eqs. (44), (46), and (55)–(58) from Ref. 21 and assuming that Knudsen number $K = 0$ (i.e., that the cylinders and the distances between them are large compared to the molecular mean free path). This results in the following expressions:

$$\alpha_\infty = 2 - \phi, \quad (27a)$$

$$\sigma = \frac{1}{a^2} \frac{16\eta(1 - \phi)}{(-2 \ln(1 - \phi) - 2\phi - \phi^2)}, \quad (27b)$$

$$\kappa_0' = \frac{2\eta}{\sigma}, \quad (27c)$$

$$\Lambda = a \frac{(2 - \phi)\phi}{2(1 - \phi)}, \quad (27d)$$

$$\Lambda' = a \frac{\phi}{(1 - \phi)}. \quad (27e)$$

Due to symmetry, only a quarter of the 3D geometry was modeled. Both the 3D and 2D models give reasonably close prediction. For example, at 300 Hz, the mean error is 14.6% for the 2D FE model compared to measurements while it is 13.2% for the 3D FE model. The error was first calculated for each angle as the magnitude of the difference between the measured and the predicted values of the normalised pressure divided by the measured value. After that, it was averaged over all angles and expressed in per cent to get the mean error. This confirms that the supporting plates are insignificant in terms of the acoustic performance of the OA and validates the numerical model.

Having validated the numerical model, the semi-analytical model was then validated indirectly, i.e., by

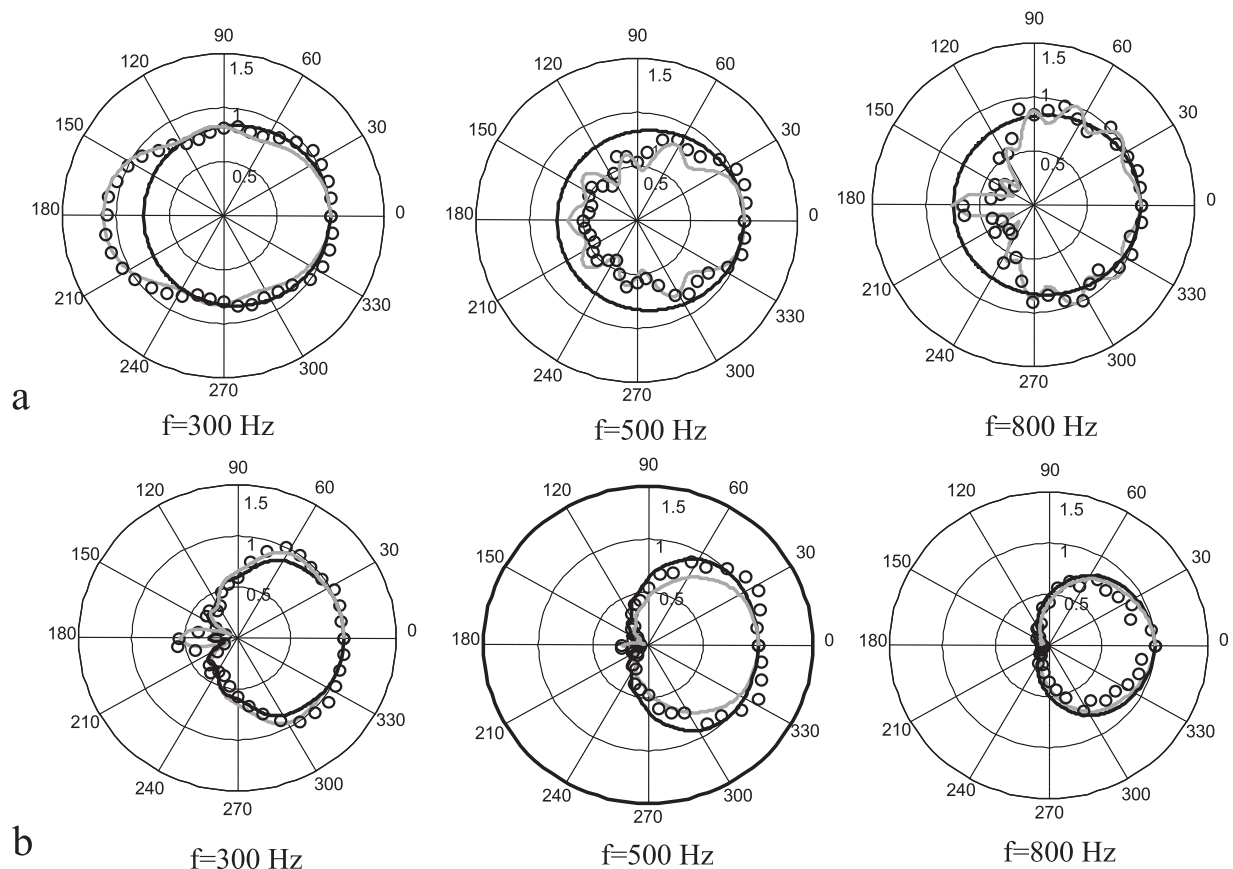


FIG. 9. Normalised *rms* pressure distribution in the “free” field (a) and around OA (b) for frequencies 300 Hz, 500 Hz, 800 Hz. Black line: 2D FEM model. Grey line: 3D FEM model. Circles: Measurements. Pressure is normalised to front microphone reading in all cases.

showing that its predictions are very close to 2D FE model. The normalised *rms* pressure predictions of the semi-analytical model presented in Sec. IV for the hollow absorbing cylinder and the OA are compared to those of 2D FE model in Figure 10. Unlike Sec. IV, the calculations were performed for a cylindrical incident wave, i.e., a point source as opposed to plane waves.

With the 2D model now validated against measurement, it can be used with some confidence to investigate further the performance of the device, for example, by considering the reduction of reflections from the OA when compared to the porous cylinder. As such, distributions of pressure for both cases are shown in Figure 11 for four frequencies. A point source with free space reference power per unit length 1 W/m is assumed, the distance between the OA centre and the source is 261 cm. The reduction of “ripples” in front of the structure is visible for all frequencies, which confirms that front reflections from the OA are less than from a porous cylinder of the same size. Pressure values behind the structure are similar, which means that both provide good shadow. The differences between the two structures are more pronounced at lower frequencies in the range which the OA was optimised for and where conventional absorber materials are known to be less effective.

VII. ANALYSIS OF LOSSES IN THE MATCHING LAYER

Losses in the matching layer (here, composed of small cylinders) will affect the OA performance if viscous and thermal boundary layer skin depths, defined as $\delta_\nu = \sqrt{2\eta/(\omega\rho_0)}$ and $\delta_T = \sqrt{2\eta/(\omega N_{pr}\rho_0)}$,²² are not negligible compared to the radius of the small scatterers and the spacing between them. This implies that the performance of the absorber could be enhanced if the matching layer is multi-functional, i.e., it provides the desired wave speed profile whilst also providing some absorption. For this reason, losses in the matching layer have also been modeled as an extension to the main aims of this paper.

To account for viscous and thermal losses in the matching layer, it was treated as a rigid porous material with effective properties $\alpha(r)$ and $\kappa(r)$ defined by Eq. (23); which in the case of no losses are reduced to Eq. (6). Assuming cylindrical scatterers, Eq. (27) was used to calculate the

parameters of the medium. First, the influence of losses on the performance of the experimental device is estimated (although comparisons between the semi-analytical and 2D FE models presented in Sec. IV already indicate that losses are weak). The strength of the effect depends on the cylinder radius a , the filling fraction F , and the frequency. The highest filling fraction (0.44) in the innermost layer is achieved using cylinders with radius 0.635 cm (Table I). Half of the distance between the cylinders in this layer is 0.21 cm. At the lowest working frequency of 300 Hz, $\delta_\nu = 0.013$ cm and $\delta_T = 0.015$ cm, which is more than 10 times smaller than the half of the distance between the cylinders. This means that the effect of losses is weak in the whole working frequency range. However, if smaller scattering elements are used in the matching layer, losses might have noticeable implications on the design and should therefore be accounted for.

As an example, consider a device with outer radius $R = 75$ cm and with matching layer composed of cylinders with radius $a = 0.05$ cm. The wavenumber in the lossy matching layer is complex valued, so condition (8) was applied to its real part (see Eq. (28)). This approximation is accurate only if the imaginary part of the wavenumber is small compared to the real one. In the calculation, a continuous profile of the matching layer is assumed which is justified by the small cylinder size. The absorbing core radius R_c was calculated by matching the absolute value of layer characteristic impedance at this location with that of the mineral wool at 1000 Hz. This results in $R_c = 58.4$ cm. A filling fraction profile in the matching layer with losses taken into account is compared to that for the lossless layer in Figure 12(a). It can be seen that the calculated filling fraction profile for a lossy layer is less steep than that of the lossless one: the maximum filling fraction achieved $r = R_c$ is 0.41 while in the lossless matching layer, this would be 0.65. The maximum value of the ratio $Im(k(r))/Re(k(r))$ achieved at $r = R_c$ is 0.09; its smallness justifies the use of condition

$$Re(k(r))R = k_0 Re\left(\sqrt{\alpha_p(r)/\kappa_p(r)}\right)R = k_0 r, \quad (28)$$

which was used to calculate the filling fraction profile $F(r)$ in the matching layer. The filling fraction dependence on the radius obtained from Eq. (28) (with effective properties

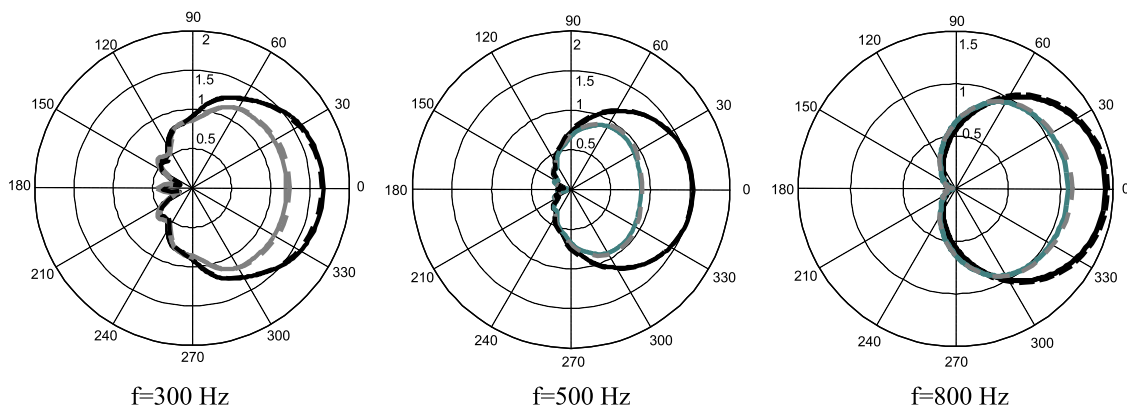
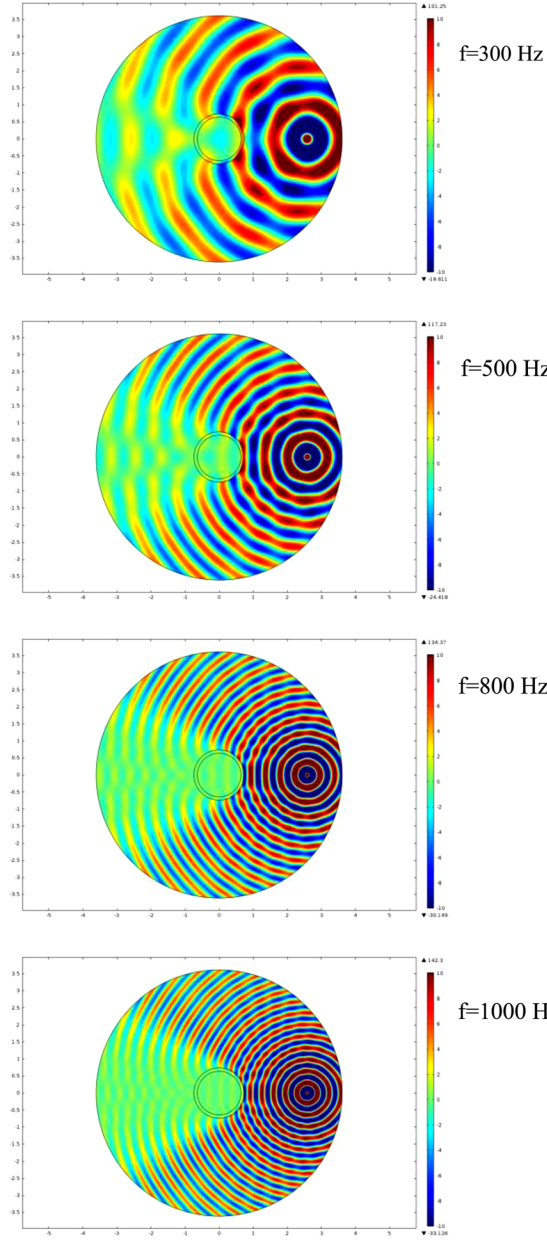


FIG. 10. Angular distribution of normalised *rms* pressure on the surface of the hollow porous cylinder (black lines) and OA (grey lines). Solid lines: 2D FE model. Dashed lines: semi-analytical model.

Hollow porous cylinder



OA

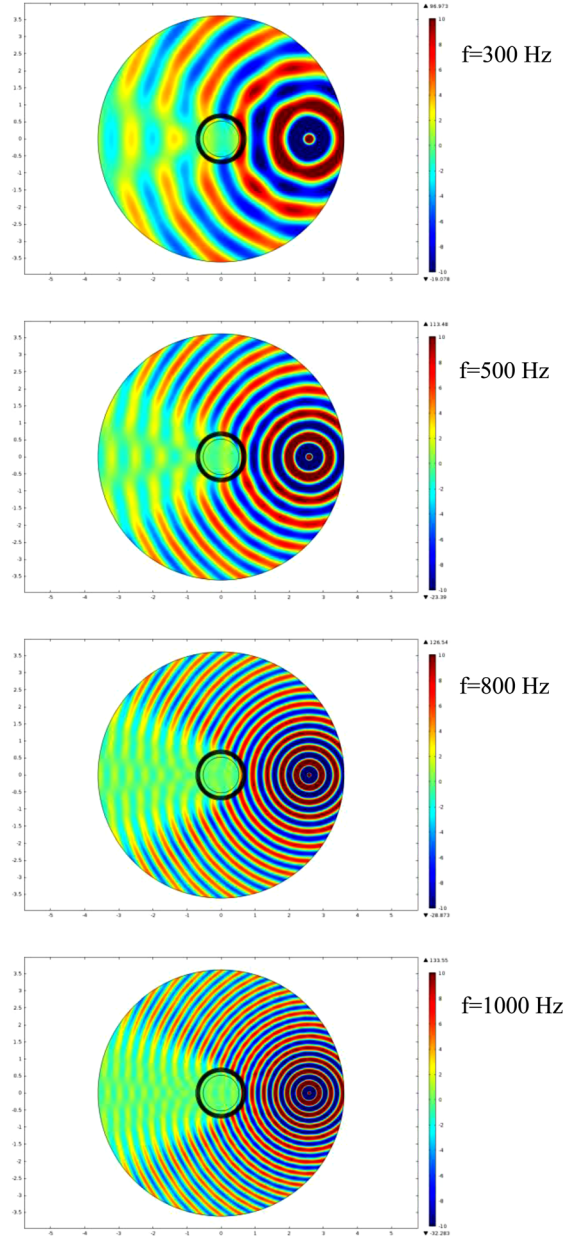


FIG. 11. Pressure distribution around the hollow porous cylinder (left) and OA (right) in Pascals.

defined by Eqs. (27) assuming $\phi(r) = 1 - F(r)$) is implicit, which complicates the solution of the equation for the pressure in the matching layer. With no losses accounted for, Eq. (5) was easily reduced to Eq. (15) and was solved using standard numerical methods. With the losses taken into account, equations of momentum and mass conservation in the matching layer are solved using the state vector formalism together with Peano series expansion.²³ First, a system of equations for Fourier components of pressure in the matching layer $p_m(r)$ (see Eq. (4)), and, for normalised radial velocity, $v_m(r)$ (so that $rv_r = \sum_{m=-\infty}^{\infty} v_m(r)e^{im(\theta+\pi/2)}$) is derived

$$W'(r, m) - A(r, m)W(r, m) = 0, \quad (29)$$

where $W(r, m) = \langle p_m(r) v_m(r) \rangle$ and

$$A(r, m) = \frac{i}{r} \begin{bmatrix} 0 & \omega \rho_0 \alpha(r) \\ \frac{\omega r^2}{\rho_0 c^2 \kappa(r)} - \frac{m^2}{\omega \rho_0 \alpha(r)} & 0 \end{bmatrix}. \quad (30)$$

System of equations (29) is, of course, equivalent to the second order differential equation (5) for Fourier components of pressure. The solution of system (29) at the outer interface $r = R$ takes the following form:

$$W(R, m) = M(m)W(R_c, m), \quad (31)$$

here M is the so called matricant,²³ which relates the value of the state vector $W(R_c, m)$, at the interface with porous absorber to its value $W(R, m)$. Since $A(r, m)$ is r dependent, i.e., the matching layer is not homogeneous, and $A(r, m)$

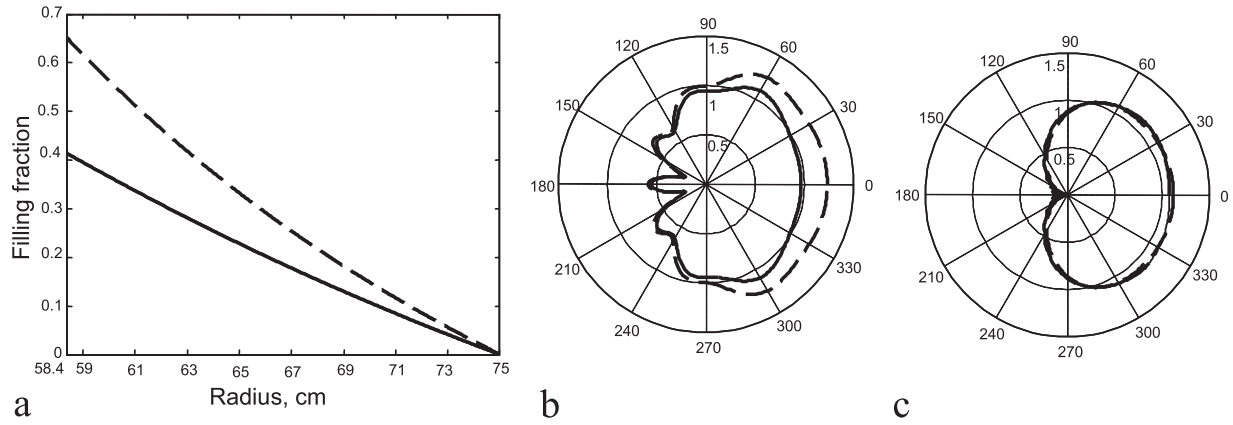


FIG. 12. Comparison of calculations with and without losses in the matching layer taken into account. Radius of the cylinders in the matching layer is 0.05 cm. Filling fraction profile (a) and angular distribution of normalised *rms* pressure on the surface of the OA with a porous core at 300 Hz (b) and at 1000 Hz (c). Solid lines: losses, dashed lines: no losses.

does not commute for different values of r , i.e., $[A(r, m), A(r', m)] \equiv A(r, m)A(r', m) - A(r', m)A(r, m) \neq 0$, where $R_c \leq r, r' \leq R$, $r \neq r'$, the matricant does not contain matrix exponentials or products of matrix exponentials. It is defined by the so-called multiplicative integral satisfying the Peano expansion.^{23–25} This avoids any problems related to lack of discretization when a material with continuously varying properties is approximated by a medium with piecewise constant properties. The Peano series reads as

$$M(m) = I + \int_{R_c}^R A(r, m) dr + \int_{R_c}^R A(r, m) \left(\int_{R_c}^r A(\zeta, m) d\zeta \right) dr + \dots, \quad (32)$$

and the evaluation of $M(m)$ is performed via the iterative scheme $M(m)^{\{0\}} = I$,

$$M(m)^{\{j\}} = I + \int_{R_c}^R A(r, m) M(m, r)^{\{j-1\}} dr, \quad (33)$$

where I is an unit matrix and $\lim_{j \rightarrow \infty} M(m)^{\{j\}} = M(m)$. The application of boundary conditions for pressure and velocity at interfaces $r = R_c$ and $r = R$, taking into account the first of Eq. (29), i.e., $v_m(r) = \frac{r p'_m(r)}{i \omega \rho_0 \alpha(r)}$, yields the state vectors $W(R_c, m) = L_m^i D_m$ and $W(R, m) = L_m^e B_m + S_m$ where

$$L_m^e = \begin{bmatrix} H_m(k_0 R) \\ \frac{R}{i \omega \rho_0} H'_m(k_0 R) \end{bmatrix}, \quad (34a)$$

$$S_m^e = \begin{bmatrix} J_m(k_0 R) \\ \frac{R}{i \omega \rho_0} J'_m(k_0 R) \end{bmatrix}, \quad (34b)$$

$$L_m^i = \begin{bmatrix} H_m(k_p R_c) + a_m J_m(k_p R_c) \\ \frac{R_c}{i \omega \rho_0 \alpha_p} (H'_m(k_p R_c) + a_m J'_m(k_p R_c)) \end{bmatrix}, \quad (34c)$$

and scattering coefficients B_m are defined in Eq. (12b), $a_m = \frac{C_m}{D_m}$, C_m , and D_m are defined in Eq. (17). Coefficients a_m depend on the boundary conditions imposed at the porous layer backing $r = R_i$. In case of an open porous layer,

$$a_m = \frac{J_m(k_0 R_i) H'_m(k_p R_i) - \alpha_p H_m(k_p R_i) J'_m(k_0 R_i)}{\alpha_p J_m(k_p R_i) J'_m(k_0 R_i) - J_m(k_0 R_i) J'_m(k_p R_i)}. \quad (35)$$

Finally, introducing Eqs. (34a)–(34c) in (31), the system of equations for coefficients B_n and D_n is derived

$$M(m) L_m^i D_m - L_m^e B_m = S_m, \quad (36)$$

which is solved for each frequency and each value of m . The solution provides the set of scattering coefficients B_m required to calculate pressure around the structure.

The angular normalised pressure distribution on the device surface calculated with and without and without losses taken into account are shown in Figures 12(b) and 12(c) for frequencies 300 Hz and 1000 Hz. The calculations for lossless profile have been performed assuming $R_c = 62.5$ cm to be consistent with Secs. II–VII.

It is clear that the effect of losses is stronger at low frequencies due to growth of boundary layer skin depths. At 300 Hz: $a/\delta_\nu = 3.9$, $a/\delta_T = 3.3$ and the half of the minimum distance between the cylinders is 0.019 cm which is less than 1.5 times bigger than δ_ν . As shown in Figure 12(b), the OA with lossy matching layer increases the efficiency of the absorber at 300 Hz. It should be noted, however, that the lossy matching layer is more than 4 cm thicker than the lossless one, which could contribute to the effect (the outer dimensions remain the same however).

VIII. CONCLUSIONS

An omnidirectional absorber comprised of a graded index metamaterial impedance matching layer and an absorbing porous core has been modelled, built, and tested. The graded index array was created using 6 rows of sub-wavelength in size cylinders with varying filling fraction. The design is based on a 2D semi-analytical scattering model and 2D and 3D FE models. It has been predicted

theoretically and confirmed experimentally that the matching layer offers an improvement in absorption, even when the ideal smooth grading is approximated with just six layers and even when the device radius is comparable to the wavelength of sound, it is still more effective than a porous absorbing cylinder of the same size without a matching layer.

The device with a central cavity (hollow absorbing core) is nearly as effective as that with the full core. Experiments have been performed using 10 cm open layer of mineral wool. Designs with both open and rigidly backed porous layers have been modelled and are proved effective even when absorber thickness is less than 1/4 of sound wavelength. This suggests that the absorber can be arranged around existing structures and, hence, would not require a significant amount of space. A semi analytical method has been used to account for viscous and thermal losses in the metamaterial matching layer. The calculations confirm that the effect of losses can be significant when the size of the matching layer basic units or the distance between them is comparable to viscous and thermal boundary layer skin depths, i.e., when small elements are used to achieve a smooth profile in the matching layer. It is shown, that introduction of losses in the matching layer can improve the absorber performance at low frequencies.

ACKNOWLEDGMENTS

The work was supported by DSTL, UK, Contract No. DSTLX1000063985. O.U. is grateful to Region Pays de la Loire for the support of her visit to Le Mans University, France.

- ¹E. E. Narimanov and A. V. Kildishev, "Optical black hole: Broadband omnidirectional light absorber," *Appl. Phys. Lett.* **95**, 041106 (2009).
- ²T. P. Martin, M. Nicholas, G. J. Orris, L.-W. Cai, D. Torrent, and J. Sanchez-Dehesa, "Sonic gradient index lens for aqueous applications," *Appl. Phys. Lett.* **97**, 113503 (2010).
- ³T. M. Chang, G. Dupont, S. Enoch, and S. Guenneau, "Enhanced control of light and sound trajectories with three dimensional gradient index lenses," *New J. Phys.* **14**, 035011 (2012).
- ⁴V. Romero-Garcia, R. Pico, A. Cebrecos, V. J. Sanchez-Morcillo, and K. Staliunas, "Enhancement of sound in chirped sonic crystals," *Appl. Phys. Lett.* **102**, 091906 (2013).
- ⁵J. Zhu, Y. Chen, X. Zhu, F. J. Garcia-Vidal, X. Yin, W. Zhang, and X. Zhang, "Acoustic rainbow trapping," *Sci. Rep.* **3**, 1728 (2013).

- ⁶V. V. Krylov and R. E. T. B. Winward, "Experimental investigation of the acoustic black hole effect for flexural waves in tapered plates," *J. Sound Vib.* **300**, 43–49 (2007).
- ⁷R.-Q. Li, X.-F. Zhu, B. Liang, Y. Li, X.-Y. Zou, and J.-C. Cheng, "A broadband acoustic omnidirectional absorber comprising positive-index materials," *Appl. Phys. Lett.* **99**, 193507 (2011).
- ⁸Q. Wei, Y. Cheng, and X. J. Liu, "Acoustic omnidirectional superabsorber with arbitrary contour," *Appl. Phys. Lett.* **100**, 094105 (2012).
- ⁹A. Climente, D. Torrent, and J. Sanchez-Dehesa, "Omnidirectional broadband acoustic absorber based on metamaterials," *Appl. Phys. Lett.* **100**, 144103 (2012).
- ¹⁰B. Brouard, D. Lafarge, and J.-F. Allard, "A general method of modelling sound propagation in layered media," *J. Sound Vib.* **183**, 129–142 (1995).
- ¹¹S. Mahasranon, K. V. Horoshenkov, A. Khan, and H. Benkreira, "The effect of continuous pore stratification on the acoustic absorption in open cell foams," *J. Appl. Phys.* **111**, 084901 (2012).
- ¹²C. Boutin, "Acoustics of porous media with inner resonators," *J. Acoust. Soc. Am.* **134**, 4717–4729 (2013).
- ¹³C. Lagarrigue, J. P. Groby, V. Tournat, O. Dazel, and O. Umnova, "Absorption of sound by porous layers with embedded periodic arrays of resonant inclusions," *J. Acoust. Soc. Am.* **134**, 4670–4680 (2013).
- ¹⁴J. Mei, Z. Liu, W. Wen, and P. Sheng, "Effective mass density of fluid-solid composites," *Phys. Rev. Lett.* **96**, 024301 (2006).
- ¹⁵B. H. Song and J. S. Bolton, "A transfer-matrix approach for estimating the characteristic impedance and wave numbers of limp and rigid porous materials," *J. Acoust. Soc. Am.* **107**(3), 1131–1152 (2000).
- ¹⁶D. L. Johnson, J. Koplik, and R. Dashen, "Theory of dynamic permeability and tortuosity in fluid-saturated porous media," *J. Fluid Mech.* **176**, 379–402 (1987).
- ¹⁷D. Lafarge, P. Lemarinier, J. F. Allard, and V. Tarnow, "Dynamic compressibility of air in porous structures at audible frequencies," *J. Acoust. Soc. Am.* **102**, 1995–2006 (1997).
- ¹⁸F. P. Mechel, "Absorption cross section of absorber cylinders," *J. Sound Vib.* **107**, 131–148 (1986).
- ¹⁹W. Lu, J. Jin, Z. Lin, and H. Chen, "A simple design of an artificial electromagnetic black hole," *J. Appl. Phys.* **108**, 064517 (2010).
- ²⁰F. P. Mechel, "On sound absorption of finite-size absorbers in relation to the radiation impedance," *J. Sound Vib.* **135**, 225–262 (1989).
- ²¹O. Umnova, D. Tsiklauri, and R. Venegas, "Effect of boundary slip on the acoustical properties of microfibrinous materials," *J. Acoust. Soc. Am.* **126**, 1850–1861 (2009).
- ²²J.-F. Allard and N. Atalla, *Propagation of Sound in Porous Media: Modelling Sound Absorbing Materials*, (John Wiley & Sons Ltd., Chichester, 2009), p. 55.
- ²³M. C. Pease, *Methods of Matrix Algebra* (Academic Press, New-York, 1965), Chaps. VI–VII.
- ²⁴C. Baron, "Le développement en série de Peano du matricant pour l'étude de la propagation des ondes élastiques en milieux à propriétés continuellement variables (Matricant Peano series development to study elastic waves propagation in media with continuously varying properties)," Ph.D. dissertation (Université de Bordeaux I, 2005) (in French).
- ²⁵G. Peano, "Intégration par série des équations différentielles linéaires (Integration of linear differential equations by series expansion)," *Math. Ann.* **32**, 450–456 (1888) (in French).